Richter, Steffen; Rebarz, Mateusz; Herrfurth, Oliver; Espinoza, Shirly;
Schmidt-Grund, Rüdiger; Andreasson, Jakob

Broadband femtosecond spectroscopic ellipsometry

Original published in:	Review of scientific instruments / American Institute of Physics. - [S.l.] : American Institute of Physics. - 92 (2021), 3, art. 033104, 14 pp.
Original published:	2021-03-04
ISSN:	1089-7623
DOI:	10.1063/5.0027219
[*Visited:*	2022-02-23]

Review of Scientific Instruments ARTICLE scitation.org/journal/rsi

Broadband femtosecond spectroscopic ellipsometry

Cite as: Rev. Sci. Instrum. 92, 033104 (2021); doi: 10.1063/5.0027219
Submitted: 27 August 2020 • Accepted: 31 January 2021 •
Published Online: 4 March 2021

Steffen Richter,[1,a),b)] Mateusz Rebarz,[1] Oliver Herrfurth,[2] Shirly Espinoza,[1,a)] Rüdiger Schmidt-Grund,[2,3] and Jakob Andreasson[1]

AFFILIATIONS

[1] ELI Beamlines/Fyzikální ústav AV ČR, v.v.i., Za Radnicí 835, 25241 Dolní Břežany, Czech Republic
[2] Universität Leipzig, Felix-Bloch-Institut für Festkörperphysik, Linnéstr. 5, 04103 Leipzig, Germany
[3] Technische Universität Ilmenau, Institut für Physik, Weimarer Str. 32, 98693 Ilmenau, Germany

[a)] **Authors to whom correspondence should be addressed:** steffen.richter@liu.se and shirly.espinoza@eli-beams.eu
[b)] **Present address:** Linköpings Universitet, Institutionen för Fysik, Kemi och Biologi, 58183 Linköping, Sweden.

ABSTRACT

We present a setup for time-resolved spectroscopic ellipsometry in a pump–probe scheme using femtosecond laser pulses. As a probe, the system deploys supercontinuum white light pulses that are delayed with respect to single-wavelength pump pulses. A polarizer–sample–compensator–analyzer configuration allows ellipsometric measurements by scanning the compensator azimuthal angle. The transient ellipsometric parameters are obtained from a series of reflectance-difference spectra that are measured for various pump–probe delays and polarization (compensator) settings. The setup is capable of performing time-resolved spectroscopic ellipsometry from the near-infrared through the visible to the near-ultraviolet spectral range at 1.3 eV–3.6 eV. The temporal resolution is on the order of 100 fs within a delay range of more than 5 ns. We analyze and discuss critical aspects such as fluctuations of the probe pulses and imperfections of the polarization optics and present strategies deployed for circumventing related issues.

I. INTRODUCTION

Ellipsometry is a well-established method to obtain thin-film properties and material optical constants, which, in particular, allows gaining insights into the electronic structure of materials. Achieving a temporal resolution below a nanosecond in an ellipsometry experiment is not possible through standard ellipsometer technology but requires different approaches such as streak-camera detection[1] or pump–probe schemes.[2–6] Although streak cameras in principle allow time-resolved measurements even with continuous-wave white light sources, this approach is still very limited in terms of temporal resolution and suffers from high noise levels. The pump–probe technique has historically been restricted mostly to single-wavelength probes and, in the case of ellipsometry, has suffered from experimental instabilities and related uncertainties. Consequently, time-resolved optical spectroscopy at solids has largely been carried out through transient reflectance and transmittance measurements.[2,6,7] Two main problems have remained for the correct determination of transient optical constants and, subsequently, a better understanding of excited solids: On one hand, a bare transient reflectance or transmittance measurement in principle does not allow distinction between changes in absorption (extinction coefficient) and refractive index. On the other hand, single-wavelength probes leave too many degrees of freedom open in order to reliably apply physical models. As an example, it is impossible to properly distinguish whether a rise in absorption, measured at a single wavelength in the bandgap of a semiconductor, is caused by bandgap collapse, free charge carriers, or activated defects. Model assumptions need to be applied, often blindly, and cannot be proven correct or wrong. These principal limitations become particularly challenging when different scattering and relaxation processes occur simultaneously and need to be distinguished.[8,9] Access to a complex-valued response function is necessary. Obtaining complex reflectance spectra (including amplitude and phase shift) directly is only

possible for frequencies not higher than the THz range by, e.g., time-domain spectroscopy.[10] For visible (VIS) light, a workaround is pump–probe measurements with at least two different angles of incidence.[11–14] Later, actual ellipsometry with narrow-wavelength-band probes was successfully applied.[15–17] Nowadays, commercial laser technology has matured sufficiently to make supercontinuum generation (SCG) in transparent crystals a versatile broadband optical probe with femtosecond laser pulses.[18,19] This opens the path for ultrafast pump–probe spectroscopic ellipsometry.

In recent years, the development of time-resolved ellipsometry has been approached through various schemes, employing either imaging techniques[20–23] or spectroscopic means,[24,25] in some cases with interferometric detection schemes.[26] Others have focused on transient circular dichroism, even employing heterodyne detection schemes, but did not aim for full ellipsometric information.[27,28] The related fields of application reach from spectroscopy of excited charge carriers, phonons, and many-body effects,[21,29–32] over shock waves,[26] to melting and material ablation.[20,22,33] However, reports on successful experiments using spectroscopic time-resolved ellipsometry are rare, pointing at a gap between proof-of-principal capabilities of reported setups and their practical ability to reliably generate high-quality spectroscopic–ellipsometry data from pump–probe experiments. In this paper, we present a setup for pump–probe ellipsometry with femtosecond white light pulses ranging from near-infrared (NIR) through the visible (VIS) to the near-ultraviolet (NUV). It is capable of obtaining pump-induced transient changes in the linear optical response of a wide range of materials and sample types. We detail the setup and related data-reduction schemes and discuss limitations and extensions.

The setup presented here, and its further developments, is available for the international scientific community as a user instrument at the Extreme Light Infrastructure (ELI) Beamlines facility in the Czech Republic, with access granted based on an open application procedure.[34]

II. EXPERIMENTAL SETUP

A. Components and measurement scheme

A scheme of the setup for time-resolved ellipsometry is shown in Fig. 1. The pump–probe system is based on an amplified titanium–sapphire femtosecond laser with its fundamental mode at 800 nm and a repetition rate of 1 kHz [Coherent Astrella (35 fs, max. 6 mJ) or Spectra-Physics/Femto-Lasers Femtopower (20 fs, max. 4 mJ)]. A fraction of about 1 μJ of the fundamental beam (exact pulse energy can be set by using an attenuator) is taken for supercontinuum generation (SCG, see Sec. II B 2 for details). The generated ultrashort broadband pulses are used as a probe beam. The main part of the pulse energy is applied as a pump beam, typically after wavelength conversion by means of second or third harmonics generation (HG). An optical parametric amplifier (OPA) will enable the target wavelength to be freely selected in a wide spectral range from 200 nm to 2600 nm (Light Conversion, TOPAS). The pump pulses are propagated through a delay line based on a 1 m-long high-performance motorized linear stage (Newport IMS-LM-S), which gives up to 6.67 ns of pump–probe delay, adjustable with a temporal resolution of about 3 fs (500 nm bidirectional repeatability of the delay-line stage).

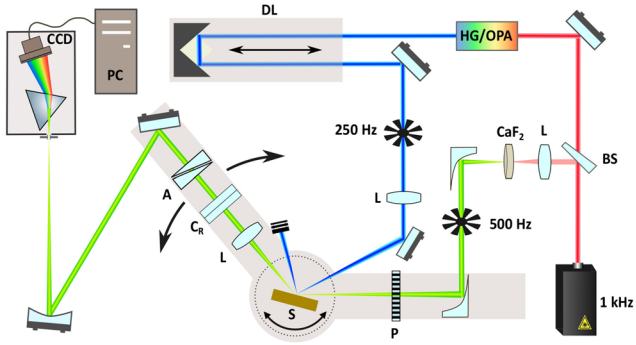

FIG. 1. Schematic view of the setup for time-resolved ellipsometry. The output of an amplified titanium–sapphire laser is split (BS) to provide white light probe pulses created by supercontinuum generation (CaF_2) and pump pulses that can be converted by means of second or third harmonic generation (HG) or, in the future, optical parametric amplification (OPA). The pump pulses are delayed by a 1 m-long delay line (DL) and focused onto the sample by a lens (L). The probe pulses are collimated and focused by 90° off-axis parabolic mirrors. The focused beam passes a broadband wiregrid polarizer (P) before reaching the sample. After reflection off the sample (S), the white light is collimated by a lens (L), goes through the compensator (C_R) and analyzer (A), and is then guided to and focused onto the spectrometer entrance by mirrors. Each individual white light pulse is detected through a spectrometer with a charge-coupled-device (CCD) camera. The chopper wheels (250 Hz, 500 Hz) allow proper detection of the reflectance-difference spectra.

The ellipsometric part of the setup, including the sample interaction point, is built on a two-circle goniometer (Huber Diffraktionstechnik GmbH), allowing reflectance and transmittance experiments at variable angles of incidence at the sample. A photograph of the equipped goniometer is depicted in Fig. 2. While the narrow-band pump pulses are focused onto the sample by a lens, the broadband probe pulses are focused by a 90° off-axis parabolic

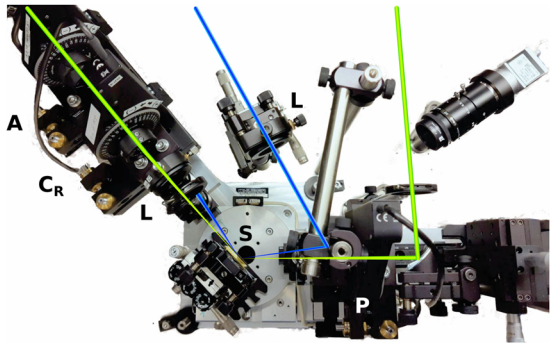

FIG. 2. Photograph of the setup goniometer. Labels and beam schematics are similar to Fig. 1. The positions of probe focusing mirror and wiregrid polarizer are fixed (right side). The sample holder can be rotated to allow a variable angle of incidence (center). Probe collimation, compensator, and analyzer are placed on a rotatable arm (left side). The reflected light is guided by mirrors to the spectrometer. The pump beam is focused through a lens and reflected by a D-shaped flat mirror (post-mounted from the top) in order to maintain an incidence angle close to the probe. A monitoring camera helps adjusting the spatial overlap of pump and probe (top right in the picture).

mirror to avoid chromatic dependencies (aberrations and chirp, see Sec. II B below). The focused white light passes through a broadband wiregrid polarizer (Thorlabs) before it is reflected off the sample. The reflected white light is collimated by a lens and guided through a compensator (superachromatic quarterwave plate, B. Halle Nachf. GmbH) and a prism analyzer (calcite Glan-type polarizer, Altechna). The polarizers and the compensator are mounted on motorized rotation stages (Thorlabs), which again are placed on tip-rotation stages to facilitate multi-axis alignment (Newport). Plane mirrors guide the light to a spectrometer (prism spectrometer, Entwicklungsbüro Stresing, or grating spectrometer, Princeton Instruments) equipped with a charge-coupled-device (CCD) camera (1024 × 64 pixel^2, dynamic range 10 000: 1, Hamamatsu Photonics/Entwicklungsbüro Stresing) working in full vertical binning mode at the 1 kHz readout rate. While the prism spectrometer provides coverage of a wide spectral range, its spectral resolution toward the NIR is rather poor. Hence, the interchangeable-grating spectrograph is used when well-resolved spectra in a given spectral range are of interest. Importantly, every change of the sample angle requires readjusting the plane mirrors between the sample goniometer and the spectrometer. Alternatively, a glass fiber can be used to guide the light to the spectrometer. However, coupling into the glass fiber is very alignment-sensitive and prone to losses.

In the described *Polarizer–Sample–Compensator–Analyzer* (PSCA) configuration, we measure the transient spectra for a series of different settings "i" of the polarization optics. In the standard case, the azimuthal angle of the compensator α_i is varied, while the polarizer and analyzer are kept fixed[35] at ±45°. The rotating compensator scheme (PSC$_R$A) has several advantages.[36] The main reason to prefer rotation of the compensator is that no polarizers need to be rotated. Rotating polarizers is problematic from two aspects: First, both the white light pulses are partially polarized[37,80] and the detection is polarization-dependent due to the potential grating and mirrors. Second, rotating a prism polarizer (in our case the analyzer) induces a beam deviation manifested mainly as a parallel shift.[38] These problems are circumvented in the rotating compensator mode.

We do not use the transient polarization-dependent intensity spectra $I_i(E, \Delta t)$ directly but rather the reflectance-difference spectra,

$$\left(\frac{\Delta R(E,\Delta t)}{R^0(E)}\right)_i = \left(\frac{R^p(E,\Delta t)}{R^0(E)} - 1\right)_i, \quad (1)$$

where $R^0(E)$ and $R^p(E, \Delta t)$ are the reflectances as a function of photon energy E for the steady and pumped states, respectively, and Δt is the pump–probe delay. The reason for this strategy is that the individual white light probe pulses vary among each other in both intensity and spectrum. Hence, the light source is not stable within the time of one revolution of the polarization-optical components (here, the compensator). This distinguishes pump–probe ellipsometry from conventional stationary ellipsometry instruments. Fluctuations of the white light spectra are caused by laser fluctuations (SCG is a highly nonlinear process) and the movement of the CaF_2 crystal used for SCG (see Subsection II B 2 below). Furthermore, kHz CCD-readout inevitably comes with high noise levels, and the warm-up of the CCD camera during the fast readout[39] additionally affects the level of background counts, which increases

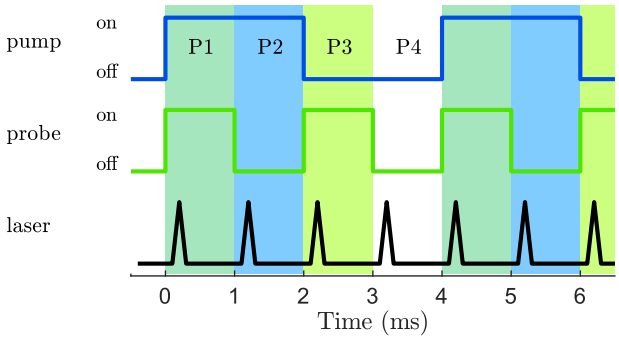

FIG. 3. Schematic representation of the two-chopper scheme with 1 kHz laser pulse repetition. The pump beam is chopped with frequency f_1 = 250 Hz and the probe with f_2 = 500 Hz. This creates four phases of *pump and probe* (P1), *pump only* (P2), *probe only* (P3), and *dark* (P4).

the absolute number of measured intensity counts. We circumvent these problems by applying a two-chopper scheme, as depicted in Fig. 3 (cf. also Fig. 1). The pump is guided through a chopper wheel running at f_1 = 250 Hz, while the probe passes through a chopper wheel running at f_2 = 500 Hz. Repeatedly, four different subsequent intensity signals are measured: *pump and probe* (P1), *pump only* (P2), *probe only* (P3), and *dark* (P4). Hence, at any time, background-corrected, or even luminescence-corrected, or even luminescence-corrected *pump and probe* spectra [$R^p(E, \Delta t) \equiv I_{P1}(E, \Delta t) - I_{P2}(E, \Delta t)$] as well as *probe only* spectra [$R^0(E) \equiv I_{P3}(E, \Delta t) - I_{P4}(E, \Delta t)$], are obtained for each compensator angle α_i and pump–probe delay Δt. Thus, the detection scheme is similar to a multi-channel lock-in amplifier system. The obtained reflectance-difference spectra are processed together with reference ellipsometry spectra to obtain the time-resolved ellipsometric parameters (see Sec. IV below).

The two-chopper strategy is very effective because the described fluctuation effects occur mostly on time scales larger than a few milliseconds. Intrinsically, it makes the measurement also immune against long-term changes of the probe–pulse spectrum (e.g., due to slightly changed laser pulse compression) and enables reliable measurement over many hours. Commonly, we scan the delay line for a certain compensator angle and not vice versa because it allows faster measurements with our motorized stages. A typical scan of 36 compensator angles, 200 delay steps, and integration over 1000 four-pulse sequences can be run in about 9 h. Control of all motorized devices (motorized stages, shutters, choppers, and detector) and data acquisition are carried out by an in-house developed software written in LabView. We refer also to Refs. 31, 32, and 40 for short descriptions of the setup with partly different details.

B. Detailed aspects

1. Optical components for femtosecond spectroscopy

Propagation of a spectrally broad femtosecond pulse through materials such as glass introduces a spectral chirp due to group-velocity dispersion.[41] In order to minimize chirping of the (white light) probe pulses, reflective optics and a wiregrid polarizer on a thin glass support are chosen before the sample. Furthermore,

a wiregrid polarizer tolerates angular deviations within a range of at least ±5° without a significant drop of performance. Hence, in contrast to prisms, it can safely be used in the focused beam. All thick prisms (compensator and analyzer) are placed in the collimated beam behind the sample, so their dispersion does not affect the temporal resolution of the experiment. Nevertheless, the SCG crystal and the support of the wiregrid induce a chirp of a few hundred femtoseconds between 2.0 eV and 3.6 eV; this corresponds roughly to propagation through 3 mm of glass. As long as the measurements are carried out with a sufficiently dense pattern of delay steps, this chirp can be removed retroactively: The true zero-delay is obtained individually for each photon energy, and correct spectra are reconstructed even on chirp-affected short time scales. Typically, we define the zero-delay by the maximum slope of the pump-induced changes. This assignment is practically arbitrary. An example using an even polynomial to describe the energy dependence of the chirp is shown in Fig. 4. It should be noted that the discussed chirp does not significantly affect the temporal resolution as long as dispersion delay calculated for a given wavelength channel (pixel of the CCD camera) does not exceed the pulse duration. It can be safely assumed that each individual spectral component of the SCG probe approximately maintains the pulse length of the seed pulse.[42,43] The temporal broadening of the pump pulses due to chirp induced by the focus lens, filter, and potentially by a waveplate is rather small. On one hand, the laser output can be negatively pre-chirped; on the other hand, the rather narrow spectral bandwidth of the pump pulses reduces the problem compared to the probe pulses. Beyond

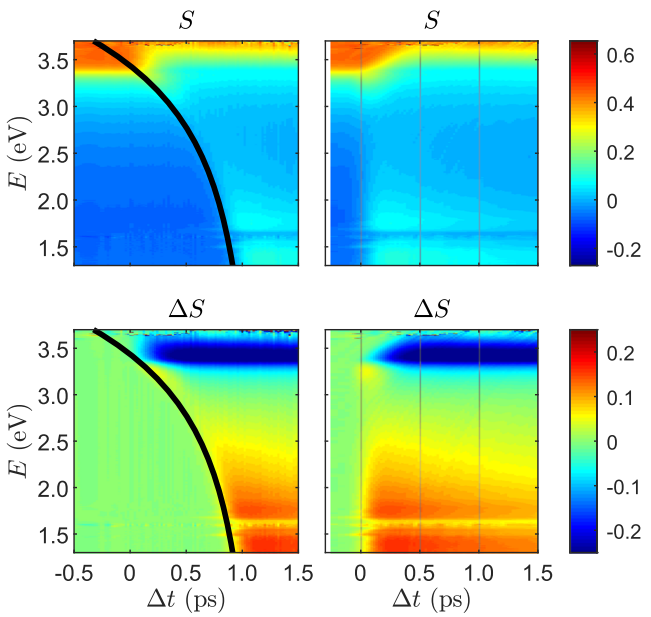

FIG. 4. Example of a retroactive correction of the probe chirp. Left-hand panels show the Müller matrix element S [cf. Eq. (4)] from a ZnO sample as directly obtained from the experiment; right-hand panels: after chirp removal by applying an even polynomial function (black line). For better visibility, bottom panels show the difference ΔS to the steady-state values. The figures also give an impression of the temporal bandwidth. The artifact around 1.55 eV originates from the scattered light off the edge of an ND filer inside the spectrometer (see the text) and needs to be excluded in further data evaluation.

chirping, lenses can induce further distortions that may affect the temporal resolution. Prepulses can arise if focusing lenses are illuminated spatially homogeneously.[44] In the present setup, such effects are of minor relevance because all beams have approximately Gaussian spatial profiles. The major sources affecting temporal resolution are discussed in Sec. II B 4.

2. Broadband transient spectroscopy

As introduced, the standard crystal used here for SCG is fluorite CaF_2. Several other materials can be used, [18] and Al_2O_3 is probably the most established one. However, the advantage of CaF_2 is that its white light continuum reaches out to about 340 nm in the NUV, while for sapphire, for example, it hardly exceeds 400 nm. The disadvantage of CaF_2 is its low thermal conductivity, and for this reason, it has to be translated continuously to prevent laser damage in the crystal window. This is done by an in-house developed motorized stage that translates the crystal in a circular pattern. This stage is mounted on a tip-rotation alignment stage as these alignment degrees of freedom are critical to avoid periodic variations of the SCG.

The supercontinuum white light still contains a significant component of the seed laser pulse, which is intense enough to easily saturate the CCD camera at the respective wavelengths. Removing this broad 800 nm line without simultaneously affecting other spectral regions of the supercontinuum is a challenging task. Currently available commercial (transmission) notch filters exhibit blocking bands, which are too narrow to effectively suppress the broad fundamental beam around 800 nm. Moreover, these filters typically also cut the NUV beyond at most 360 nm. Multi-layer reflection filters have similar limitations. The filters of choice are mostly colored-glass filters. In particular, the transmission of BG40 glass reaches comparably close to the 800 nm without cutting the UV, even further than BG39 glass, which is often used.[24] BG42, KG1, KG3, or KG5 glass on the other hand does not provide enough contrast to suppress the remaining 800 nm sufficiently without shifting the cutoff to shorter wavelengths. All mentioned colored-glass filters essentially cut all wavelengths longer than the 800 nm seed. However, it is possible to use the supercontinuum white light at wavelengths that are both shorter and longer than the seed. A way to this is covering only a part of the CCD camera inside the spectrometer by a neutral-density (ND) filter. This way, the usable spectrum can be extended in the NIR direction down to ~950 nm. The spectrum contains the diffracting imprint of the physical edge of the half-inserted filter (cf. Fig. 4), which could be optimized by a customized, nonlinearly graded ND filter. Alternative color filters are chemical solutions that, however, degrade over time.

The best position for the filters is often a trade-off between keeping the chirp to a minimum (favoring filters after the sample) and protecting the sample from the strong residual 800 nm component in the probe spectrum (requiring a filter before the sample).

3. Pump pulse generation

To optimize the excitation condition for various samples and experimental designs, the setup allows a flexible choice of the pump wavelength. Aside from the 800 nm fundamental beam of the laser, the second (400 nm) and third (267 nm) harmonics can be generated by frequency doubling and mixing in beta-barium-borate

(BBO) crystals (Eksma Optics). The advantage of this option is its simplicity and relatively high conversion efficiency. As a more universal alternative, an OPA (Light Conversion, TOPAS) will be available that allows the wavelength of the pump beam to be varied between 200 nm and 2600 nm. The conversion efficiency varies significantly for different wavelengths, and some spectral windows exhibit very low output intensity. Notably, the currently available range can also be extended toward the IR down to 12 μm by the use of difference-frequency generation (DFG, also Light Conversion).

4. Spot size and temporal bandwidth

The typical spot size that we achieve for the probe beam is around $d \approx 100$ μm in terms of $1/e^2$ diameter [Fig. 5 (a)]. In the literature, spot sizes are often given as the full-width at half maximum (FWHM), which in our case would be ~60 μm and include only 76% instead of 95% of the intensity along one dimension.[81] The pump spot is deliberately not perfectly focused on the sample surface to ensure that an approximately homogeneously pumped area is probed. Typically, the pump spot is set to be at least twice the size of the probe. The pump–probe overlap can be pre-adjusted using a camera before the strength of the transient signal is optimized. Pump and probe spot sizes are determined by knife-edge scans in the direction vertical to the plane of incidence. Exact pump power, polarization, and spot size are set by a gradient ND filter, a halfwave plate, and by adjusting the position of the focusing lens, respectively.

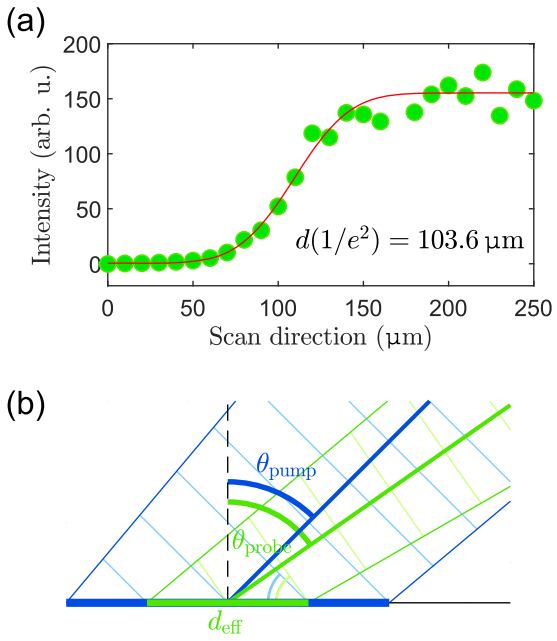

FIG. 5. (a) Knife-edge scan of the focused probe spot at the sample perpendicular to the incidence plane; all are wavelengths integrated. The fit assuming a Gaussian beam profile yields a $1/e^2$ diameter d of about 100 μm. (b) Schematic view onto the incidence plane illustrating the pump (blue) and probe (green) beams with different focal spot sizes on the sample. The wavefronts (parallel lines) are not parallel due to different angles of incidence ($\theta_{pump/probe}$) and result in different times for the pump and probe pulses to sweep over the probed area (d_{eff}).

The temporal bandwidth of the experiment depends critically on the probe spot size at the sample and the difference in the angles of incidence (θ) of the pump and probe beams: Under oblique angle (measured from the surface normal), the probe spot is elongated on the sample and becomes $d_{eff} = d/\cos(\theta_{probe})$. One end of the spot on the sample is probed at a time $t_{sweep} = \sin(\theta_{probe}) d_{eff}/c_0$ earlier than the other end (c_0 being the speed of light). This is the time it takes the probe pulse to sweep over the sample. The same is true for the pump pulse, which arrives from a different angle θ_{pump} as illustrated in Fig. 5(b). In our setup, the difference between the pump and the probe angle is ~6°, e.g., $\theta_{pump} = 54°$ and $\theta_{probe} = 60°$. This leads to a continuous shift between pump and probe arrival at different sites within the spot on the sample, which again worsens the temporal resolution. We can approximately estimate the effective temporal bandwidth as the convolution of two Gaussian intensity profiles at time $I \propto 2^{-(2t/\tau)^2}$: One describes the laser pulse with a FWHM duration τ_{pulse}. The second one with length τ_{spot} parameterizes the temporal difference of pump and probe sweeping over the probe spot area on the sample. For the convolution, it holds $\tau_{eff} = \sqrt{\tau_{pulse}^2 + \tau_{spot}^2}$. With an elongated FWHM probe spot size of 120 μm (corresponding to a 100 μm $1/e^2$ probe spot diameter and $\theta_{probe} = 60°$) and an angle difference of 6° between the pump and the probe, we get $\tau_{spot} \approx 11$ fs. With $\tau_{pulse} \approx 35$ fs, we can estimate $\tau_{eff} \approx 37$ fs. Under the same conditions, a pump–probe off-angle of 20° would result in $\tau_{spot} \approx 44$ fs and $\tau_{eff} \approx 56$ fs. Similarly, the temporal bandwidth also increases with a larger probe spot diameter. It should be mentioned that a temporal bandwidth of $\tau_{eff} \approx 37$ fs in terms of FWHM corresponds to 63 fs in terms of $1/e^2$ width. With regard to this comparison, it seems that spot sizes and temporal bandwidth are probably often underestimated in the literature.

Finally, it should be mentioned that the temporal resolution of the experiment could be improved by decreasing the entrance slit of the spectrometer. In our setup, the probe spot is imaged without magnification onto the entrance slit of the spectrometer, and the discussed oblique sweep direction of the spot at the sample (direction of the plane of incidence) is imaged perpendicular to the spectrometer entrance slit. Hence, the width of the entrance slit ultimately determines d_{eff}.

III. CALIBRATION

Operating the setup requires wavelength and ellipsometric calibration. Wavelength calibration is typically done either with a series of narrow bandpass filters (used in combination with the broadband prism spectrometer) or holmium- or didymium-doped glasses (for the grating spectrometer with a higher spectral resolution). Usually, the wavelength calibration has to be repeated after each sample exchange and subsequent optimization of coupling the light into the spectrometer.

The ellipsometric calibration consists of two basic steps:[45–47] First finding zero azimuthal angles of the polarizers and the compensator and second obtaining the compensator properties for each wavelength. The zero angles are determined through reflectance measurement off a silicon wafer (with a native oxide layer) close to Brewster's angle. For convenience, we remove all elements but one (e.g., polarizer) at the time from the beam path. In general, placing a broadband depolarizer before the polarizer, or replacing the SCG by

a reference xenon lamp, is useful for the calibration routines. Both polarizers have sufficient performance to be treated as ideal (extinction ratios $<5\cdot10^{-4}$ for the wiregrid polarizer and $2\cdot10^{-6}$ for the prism analyzer). It should be noted that prior to all measurements, all rotatable polarization optics are aligned with respect to both the tilt of the optics against the rotation axis and the tilt of the rotation axis. This can be done by tracking the back reflection of an alignment laser at a rather long distance.

An ideal quarterwave-compensator can be described by a Jones matrix,[48]

$$\hat{J}^{\mathrm{comp}} = \begin{pmatrix} 1 & 0 \\ 0 & e^{i\delta} \end{pmatrix}, \tag{2}$$

with retardance $\delta = 90^\circ$ between the two linear-polarization components parallel and perpendicular to the fast axis. However, simple zero-order quarterwave plates fulfill $\delta = 90^\circ$ only for a single wavelength. Achromatic waveplates for broadband spectroscopy consist of a series of birefringent plates. The superachromatic compensator used here consists of six birefringent plates with inclined relative orientation of their individual optic axes. Therefore, the orientation of the waveplate's fast axis depends on the wavelength. However, the retardance is close to 90° between 310 nm and 1100 nm, being exactly 90° at three particular wavelengths. Another typical non-ideality of achromatic compensator slabs is oscillations occurring in their spectral dependence.[49–51] Additionally, polarization-dependent reflection losses can induce a slight linear dichroism.[52,53] Different approaches for a Jones matrix description of non-ideal compensators have been proposed to describe retardance, potential dichroism, optical activity, and other effects[38,54–56] (see also Appendix B). Here, as the orientation of the fast axis is wavelength-dependent, it is reasonable to allow complex-valued off-diagonal entries for the Jones matrix. This way, the Jones matrix can include a rotation. Hence, the nominal zero-angle of the compensator is arbitrary, and its true, wavelength-dependent zero-angle is imprinted in the Jones matrix. It turns out that a description by a symmetric Jones matrix with complex off-diagonal entries is the best-suited one for our purposes,

$$\hat{J}^{\mathrm{comp}} = \begin{pmatrix} 1 & \tan(\psi_{\mathrm{offdiag}})e^{i\delta_{\mathrm{offdiag}}} \\ \tan(\psi_{\mathrm{offdiag}})e^{i\delta_{\mathrm{offdiag}}} & \tan(\psi_{\mathrm{diag}})e^{i\delta_{\mathrm{diag}}} \end{pmatrix}. \tag{3}$$

This was confirmed by reference measurements of the compensator using a commercial ellipsometer. Consequently, four calibration parameters have to be obtained for each wavelength to characterize the real compensator. Intrinsically, a potential off-angle of or a rotation by the analyzer could also be imprinted into those calibration parameters. A more detailed discussion can be found in Appendix B.

Example compensator revolutions and wavelength-dependent Jones matrix entries for the non-ideal compensator are shown in Fig. 6. Typically, the compensator calibration is repeated before every measurement by performing a quick scan of the compensator in the setting used for the measurement. This allows a fine calibration of the compensator based on a reference measurement of the sample at a commercial stationary ellipsometer. It should be noted that multiple forth and back reflections in the compensator cannot affect the transient experiment as long as the compensator is placed behind the sample.

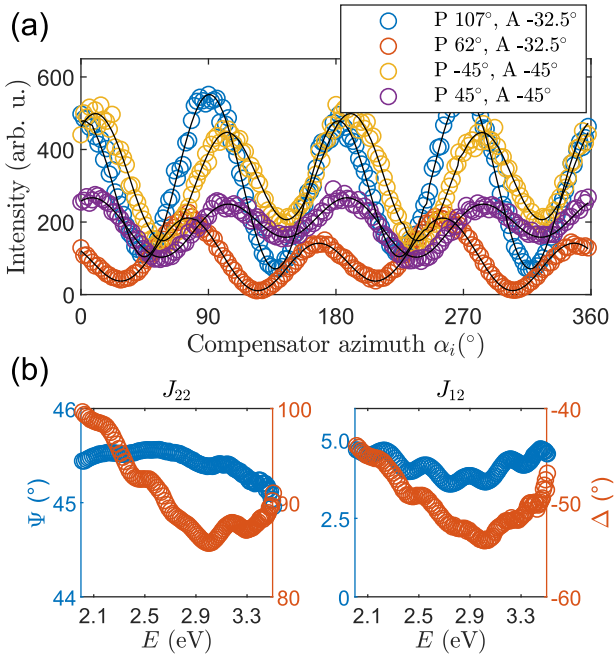

FIG. 6. (a) Exemplary data and fit as carried out for the calibration of the compensator. Data were obtained with SCG white light pulses on a silicon sample with a native oxide layer at $\theta_{\mathrm{probe}} = 70°$. Data for 3.3 eV are shown along with modeled intensities. The legend displays azimuthal angles of the polarizer (P) and analyzer (A). (b) Typical spectra of the obtained Jones-matrix entries to describe the imperfect compensator in the setup.

IV. DATA REDUCTION

The detection system allows individual spectra to be captured at a 1 kHz rate, and four subsequent spectra are required to obtain a reflectance-difference spectrum (cf. Fig. 3). Still, the data quality depends on statistical fluctuations, and in general, accumulating several hundred reflectance-difference spectra per data point is required. Obtaining the median instead of the mean $\Delta R/R^0$ of all accumulations for every wavelength channel is more robust but increases computational efforts and, hence, the dead time during data readout. In our case, it has proven advantageous to compute the mean values after clearing the data from outliers by neglecting the highest and lowest values in bands of 10% or 15%.

Further data improvement can be achieved with smoothing filters such as approximation by moving polynomials[57] or, with even better results, using kernel regression methods.[58] Such filters can be applied to both raw intensity data and to processed ellipsometric data. Furthermore, it can be useful to interpolate at the same time to an equidistant wavelength or a photon-energy grid. Thereby, spectral weighting can be controlled in subsequent modeling of the obtained ellipsometry spectra.[58]

In order to compute ellipsometric data, we use the Müller calculus and invert the linear system of equations by Moore–Penrose pseudo-inversion of a coefficient matrix that describes the polarization setup.[59,60] Details on how to compute the Müller matrix of a

pseudo-isotropic sample,

$$\begin{pmatrix} 1 & -N & 0 & 0 \\ -N & 1 & 0 & 0 \\ 0 & 0 & C & S \\ 0 & 0 & -S & C \end{pmatrix}, \tag{4}$$

from a series of intensity values I_i measured at different settings of the polarization optics (here, compensator azimuthal angle α_i) are discussed in Appendix A. The computation is applied independently for each wavelength channel and accounts for the above-detailed description of the real compensator. For the ellipsometric angles Ψ and Δ, it holds[48]

$$\Psi = \frac{1}{2}\tan^{-1}\left(\frac{\sqrt{C^2+S^2}}{N}\right), \tag{5}$$

$$\Delta = \frac{1}{2}\tan^{-1}\left(\frac{S}{C}\right), \tag{6}$$

where $0^\circ \le \Psi \le 90^\circ$ and $\Delta \in (90^\circ, 270^\circ)$ if $C < 0$ and $\Delta \in (0^\circ, 90^\circ) \cup (270^\circ, 360^\circ)$ if $C > 0$.

As mentioned above, we do not directly use the reflection intensity values $I_i(E, \Delta t)$ but the reflectance-difference signal. Consequently, we require a reference steady-state ellipsometry measurement (using a commercial ellipsometer) from the studied sample taken under the same conditions.[61] Using the reference $\Psi^0(E)$ and $\Delta^0(E)$, we can compute pseudo-intensity spectra $I_i^0(E)$, which express the intensity of reflected light for each setting of the polarization optics "i" (e.g., compensator azimuth α_i) when the unpolarized light of unit intensity [Stokes vector $(1,0,0,0)^T$] is incident at each wavelength. Consequently, for the computation of the transient ellipsometric parameters, $I_i(E, \Delta t)$ is replaced by

$$I_i(E,\Delta t) = I_i^0(E)\left(1 + \left(\frac{\Delta R(E,\Delta t)}{R^0(E)}\right)_i\right). \tag{7}$$

By this means, raw reflectance-difference data can be reduced to transient ellipsometry data. Figure 7 provides an example of reflectance-difference data $\Delta R/R^0$ for a complete revolution of the compensator ($\alpha_i = 0, \ldots, 360^\circ$). We refer again to Appendix A for details on the computation.

The next step in data reduction is the correction of the probe chirp as described in Sec. II B above (see also Fig. 4). In the final step, ellipsometric data are normally interpolated to an equidistant energy grid. An example of transient spectroscopic ellipsometry data after this last correction is shown in Fig. 8. In principle, the rotating compensator also allows obtaining depolarization information,

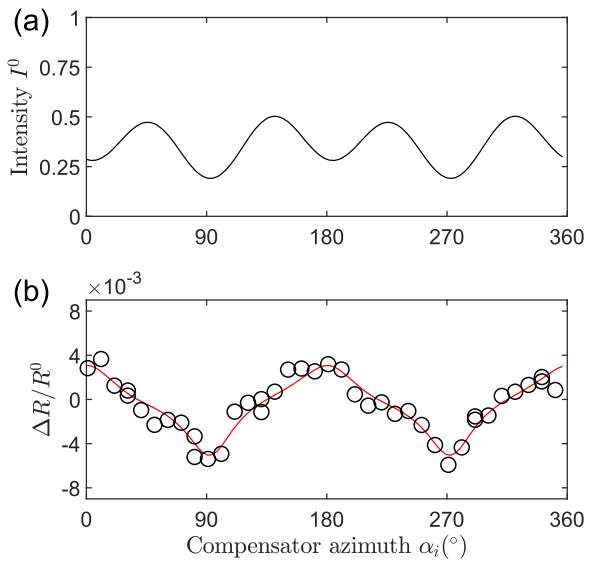

FIG. 7. Example for data reduction for a silicon sample with a 3 nm native oxide layer. Shown are data for E = 3.227 eV. (a) Normalized intensity I^0 (see the text) depending on the compensator azimuthal α_i as obtained from the reference measurement. Here, Ψ^0 = 31.601° and Δ^0 = 172.76°. (b) Measured reflectance-difference $\Delta R/R^0$ (symbols) and regression (line) for Δt = 375 fs after excitation by 800 nm pump pulses. The transient values are Ψ = 31.597° and Δ = 172.52°.

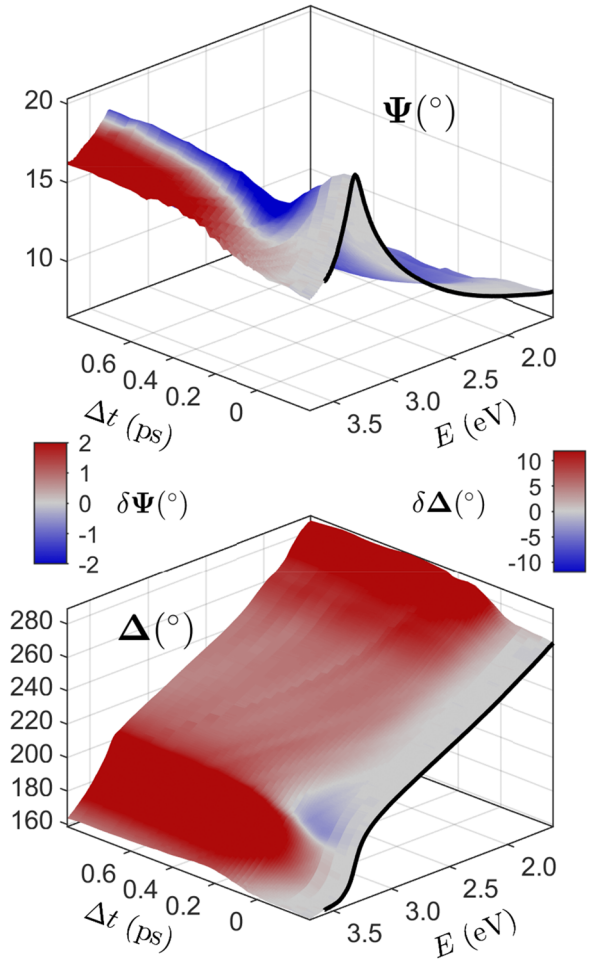

FIG. 8. Exemplary transient spectroscopic ellipsometry data from a UV-excited 35 nm-thick c-plane oriented ZnO thin film on SiO_2 at θ_{probe} = 60° during the first picosecond. The color encodes the changes with respect to the reference steady-state spectra at negative delays that are shown as black lines.

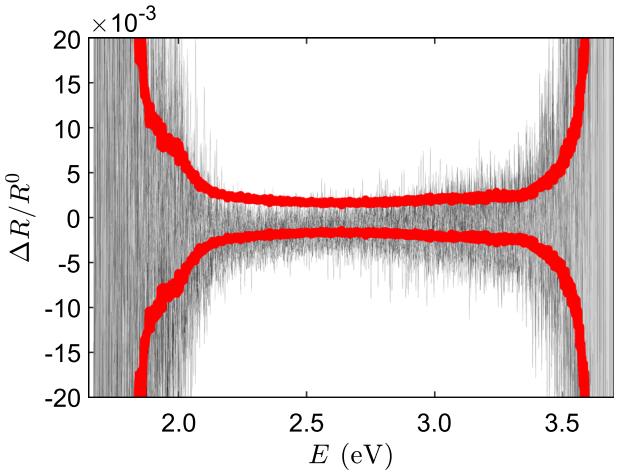

FIG. 9. Reflectance-difference spectra before the pump pulse arrives (negative Δt) for the estimation of the $\Delta R/R^0$ accuracy by its deviation from zero. Various measurements (here, 100 spectra) at different compensator angles and delays are shown piled up in different gray tones. The red lines illustrate +1 and −1 times the averaged absolute values. In the central part of the spectrum, the accuracy can be estimated to $\pm 3 \cdot 10^{-3}$. It becomes worse with vanishing light intensity as limited here by a BG40 colored-glass filter (Thorlabs FGB 37). The measurements were repeated over 500 four-pulse sequences.

which can be an indicator for changes that happen faster than the temporal bandwidth or features beyond the spectral resolution of the experiment.

A. Uncertainty estimation

Due to the modulation scheme of the experiment, the influence of systematic errors (such as uncertainties due to the imperfect polarization optics) on the difference spectra of the ellipsometric parameters is largely suppressed. The remaining uncertainty is estimated by means of Monte Carlo simulations for a given configuration (i.e., samples Ψ^0 and Δ^0, wavelength, a set of compensator angles, and quality of the reflectance-difference signal) using largest estimated uncertainty values for each parameter and intensity value I_i. This stochastic approach allows the combined systematic and stochastic uncertainties to be estimated. An example can be found in Ref. 31. Potentially erroneous input parameters are, e.g., the Jones-matrix entries that describe the compensator, the ellipsometric reference spectra, or the measured reflectance-difference spectra. Furthermore, non-idealities such as, e.g., polarizer imperfections can be included but, in our experience, hardly affect the result. As illustrated by Fig. 9, the uncertainty of the reflectance-difference signal can be estimated from measurements at negative delays, i.e., measurements of the not-yet-excited sample with the probe pulse hitting the sample before the pump. While it increases toward the ends of the accessible spectral range, an uncertainty of at most $\pm 3 \cdot 10^{-3}$ can be estimated in large parts of the spectrum.

V. DATA EVALUATION

Directly accessing the material's dielectric function (DF) is only possible if a homogeneous sample is probed. This requires that a homogeneous (non-layered) material without surface layers has been homogeneously excited by the pump. This can be fulfilled by a bulk sample or an absorbing film if the probe's penetration depth is much smaller than the film thickness. In those cases, the pseudo-DF $\langle\varepsilon\rangle$ can be directly computed from Ψ and Δ,

$$\langle\varepsilon\rangle = \sin^2(\theta_{\text{probe}})\left(1 + \left(\frac{1-\rho}{1+\rho}\tan(\theta_{\text{probe}})\right)^2\right), \tag{8}$$

where the ellipsometric ratio ρ is given as the ratio of the complex reflection coefficient for *s* and *p* polarization,

$$\rho = \frac{r_p}{r_s} = \tan(\Psi)\, e^{-i\Delta}. \tag{9}$$

In other cases, rigorous modeling of the ellipsometry spectra is required for each delay as in any ellipsometric investigation.[48] Without further prior knowledge of the shape of the DF, numerical model DFs can be obtained from simple wavelength-by-wavelength fits or using Kramers–Kronig-consistent B-spline functions.[62] Both need to be applied in a transfer matrix calculus.[63,64]

Still, pump–probe experiments at solids will often excite only surface-near regions of the sample. Ignoring the respective excitation gradient in the sample can lead to considerable artifacts. Useful strategies to circumvent this problem are to either investigate thin films on a substrate that is transparent for the pump beam[31] or to study cases where the penetration depth of the pump beam is much larger than that of the probe.[32] If this is not possible, rigorous modeling of the depth-depending excitation is required, and ambipolar diffusion needs to be taken into account.[65] Lateral motion of charge carriers can be investigated by time-resolved imaging ellipsometry.[23]

VI. DISCUSSION

The 1 kHz repetition rate of the system represents a good compromise between important features. It is low enough to allow a shot-to-shot readout and high enough to reduce the overall experimental time also for experiments when a large number of exposures are necessary. At the same time, 1 ms is a sufficiently long time between exposures for a complete relaxation of most of the solid-state processes. This is a principle requirement for the present experimental setup.

A. Limitations

The ultimate limit to data quality is determined by the pulse-to-pulse fluctuations within the set of four subsequent white light pulses in the *pump and probe*, *pump only*, *probe only*, and *dark* sequences. Figure 10 shows an example of these fluctuations by illustrating the moving standard deviation of four subsequent pulses. In the center of the spectral probe range, the moving standard deviation is similar to the $\Delta R/R^0$ noise shown in Fig. 9. The resulting ellipsometric sensitivity limit depends crucially on the configuration at which the sample is measured. As in any ellipsometry measurement, sensitivity increases close to Brewster's angle, while the reflected light intensity may decrease (and noise might increase). Sensitivities better than 0.1° in Ψ and 1° in Δ have been achieved by accumulating over 400 four-pulse sequences. A slight improvement in data quality can in general be achieved by averaging the reflectance-difference

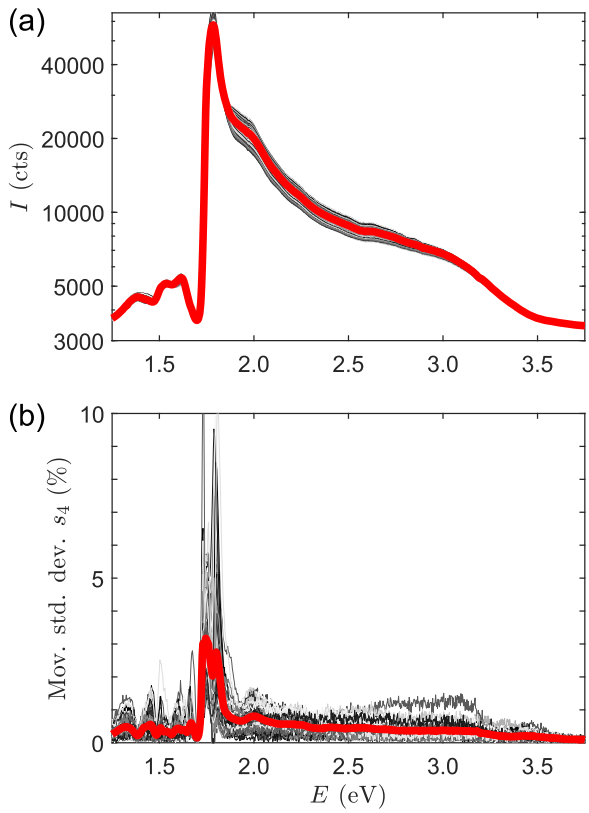

FIG. 10. Example of pulse-to-pulse fluctuations for about 4000 subsequent pulses collected (a maximum of 4000 spectra can be buffered in the camera before acquisition has to be interrupted for the readout) in a straight-through configuration. The CCD camera inside the prism spectrometer box was half-covered by a neutral-density filter; no other filter was placed into the beam. Outlier spectra deviating more than 10% from the median intensity around 2.4 eV have been removed. (a) Intensity counts for individual spectra (gray lines) and their mean (bold red line). No background correction has been applied. (b) Relative moving standard deviation of every four subsequent pulses (gray lines) as well as their mean (bold red line). Fluctuations are the strongest at energies above but close to the 800 nm seed.

spectra that are obtained at each series of four subsequent pulses, rather than calculating the reflectance-difference information from averaged intensities I_{P1}, I_{P2}, I_{P3}, and I_{P4}.[19] Nonlinearity in the CCD-camera response should not affect the measurement to first order as rather small intensity changes at the detector are obtained at any time.

Limitations with regard to the temporal resolution of the experiment have been discussed in Sec. II B. It should be added that in practice, the main limiting factors, i.e., geometrical overlap on the sample and temporal cross correlation of pump and probe pulses are often of similar magnitude. In the current configuration of the setup, the effective temporal resolution varies between 100 fs and 200 fs. In general, the meaning of a polarized light pulse ultimately changes for few-cycle pulses, where the compensator-induced retardance causes the polarization to vary between the beginning, center, and end of a pulse.[66] Such an effect cannot be resolved in the current setup, even if the temporal resolution would approach a few fs. It would be interpreted as depolarization.

A rather general question is whether Kramer–Kronig relations remain valid at arbitrarily short time scales or if causality needs to be questioned.[67,68] In this context and within the scope of a linear DF as investigated here, it is interesting to consider if the instrument would in principle allow us to measure negative ε_2 values, i.e., stimulated emission. In general, ε_2 is related to an advanced Green's function; [69] hence, negative ε_2 means that a photon is emitted prior to arrival of the triggering photon. This again typically requires a coherent field as, e.g., in a laser cavity. In contrast, that is normally not the case in a pump–probe reflection experiment. However, for a very short time, negative ε_2 has also been derived for a retarded response, and gain-based models have been successfully applied to transient reflection data.[70] With correctly carried out chirp correction, all experiments that were performed with the present setup revealed a Kramer–Kronig-consistent response. We can presently conclude that the mentioned aspects are likely to become only relevant when the temporal resolution approaches few-cycle pulses, i.e., beyond the capabilities of the present setup.

The present setup utilizes a rather slowly rotating compensator stage. Because of this, the measurement strategy is based on ensuring that a consistent series of measurements at different compensator azimuthal angles is reliably obtained even though the individual measurements are carried out with long time intervals between them. The alternative strategy would be to use a fast-spinning compensator and capture the spectral intensities during its fast revolutions. Such an approach would also waive the necessity for using reference spectra from a conventional ellipsometer.

Finally, we do not consider effects of intensity fluctuations of the pump pulses, which are typically within less than 10%. Due to the nonlinearity between pump power and pump-induced changes, tracking of the pump power would only help if all detected probe pulses are saved independently and later assigned or selected according to a constant pump power at the time. It should further be mentioned that light scattered from the pump beam (if it is in the measured spectral range) is only statistically filtered out. This requires negligible fluctuations within the four-pulse sequences. Problems can arise, e.g., when dust particles on the sample surface cause a strong detrimental stray-light signal.

B. Prospective upgrades

A number of improvements and extensions to the setup can be implemented in the future:

- A second, coupled CCD camera can be used to capture a reference signal to each individual white light pulse by splitting off a portion of the probe beam. This could ultimately beat the above-mentioned problems induced by white light fluctuations. Implementation of a spectrometer scheme using the same prism for two light paths and cameras has been initiated.
- In order to extend and stabilize the SCG, different media and seed wavelengths can be used. SCG seeded by shorter wavelengths can shift the usable wavelengths further toward the UV but requires good filters to remove the strong remaining seed (see Sec. II B above). However, SCG by

mid-infrared wavelengths can also range similarly far into the UV.[18] Available alternative media comprise a water-jet and a gas-filled hollow-core fiber (UltraFast Innovations GmbH). The latter could even enable frequency doubling of the entire SCG spectrum. However, it requires pulse compression, which is challenging if the spectrum shall not be cut in the UV. Finally, to extend the spectral range of time-resolved ellipsometry to the vacuum–UV range, another setup is being developed at ELI beamlines.[71,72]

- The sample goniometer can be equipped with a cryostat or heat cell to allow low-/high-temperature measurements. Alternatively, other sample environments (liquid or gas cells) could be employed. In all cases, effects of windows have to be examined carefully.
- For samples with slowly relaxing processes (e.g., phase changes triggered by the laser pulses that do not return within 1 ms), subsequent light pulses should pump and probe separate but adjacent points on the sample. This would require rapid sample movement[22,33] and appears more feasible than a significant reduction of the repetition rate by, e.g., chopper wheels.
- The chirp of the probe pulse is corrected retroactively. In principle, a deformable mirror or a pulse shaper could compensate the chirp actively.[73] This can be important, e.g., for very sensitive and fast processes that are altered by the first arriving long-wavelength part of the probe pulse.

VII. SUMMARY

In summary, we have presented a setup for time-resolved spectroscopic ellipsometry with a sub-picosecond temporal resolution. While the setup is not a perfect ellipsometer, it is very sensitive to any transient changes in the ellipsometric parameters and so utilizes polarization-dependent reflectance-difference spectra to obtain transient ellipsometric spectra. We have detailed critical components of the setup and strategies to combine (i) broadband spectral probing, (ii) ultrafast pump–probe techniques, and (iii) ellipsometry. The capabilities and limitations were discussed and example data are presented. First experiments were carried out with the setup in its present or an earlier state.[31,32] The setup is available for users through open access at the ELI Beamlines facility in the Czech Republic.[34]

ACKNOWLEDGMENTS

We gratefully acknowledge experimental support by Md Ziaul Hoque, Miroslav Kloz, and Martin Přeček, as well as valuable discussions with Stefan Zollner, Kurt Hingerl, and Mathias Schubert. We acknowledge the support from the projects "Advanced research using high intensity laser produced photons and particles" (ADONIS), Reg. No. CZ.02.1.01/0.0/0.0/16_019/0000789, and "Structural dynamics of biomolecular systems" (ELIBIO), Reg. No. CZ.02.1.01/0.0/0.0/15_003/0000447, from the European Regional Development Fund. Parts of this work have been funded by the Deutsche Forschungsgemeinschaft (DFG, German Research Foundation), Grant No. SFB 762, Project No. 31047526 (Project B03), and FOR 1616 (Grant No. SCHM2710/2). O.H. acknowledges the Leipzig School of Natural Sciences BuildMoNa.

APPENDIX A: DIRECT LINEAR REGRESSION FOR ELLIPSOMETRIC DATA REDUCTION

In order to compute Müller matrix elements from measured intensity values, we utilize Moore–Penrose pseudo-inversion of a setup-related matrix for each photon energy independently.

1. General formalism

We assume unpolarized light [Stokes vector $\vec{S}^0 = (I^0, 0, 0, 0)^{\mathrm{T}}$] incident on a polarization state generator [Müller matrix $\hat{M}^{\mathrm{prep}}$], i.e., a polarizer followed by a compensator or, in our case, only a polarizer. The light is reflected off the sample ($\hat{M}^{\mathrm{sample}}$) and propagates through a polarization state analyzer ($\hat{M}^{\mathrm{det}}$), i.e., a compensator followed by an analyzer. A partial measurement "i" at a certain photon energy and given azimuthal angles of the polarizer, analyzer, and compensator(s) yields intensity I_i, which is the first element of the Stokes vector behind the polarization state analyzer. It holds

$$I_i = \sum_{j,k=1,\ldots,4} M_{1k}^{\mathrm{det},i} M_{kj}^{\mathrm{sample}} M_{j1}^{\mathrm{prep},i}. \tag{A1}$$

The Müller matrices $\hat{M}^{\mathrm{prep}} = \hat{M}^{\mathrm{comp1}}\hat{M}^{\mathrm{pol}}$ and $\hat{M}^{\mathrm{det}} = \hat{M}^{\mathrm{ana}}\hat{M}^{\mathrm{comp2}}$ representing the polarization optics shall include rotations of the respective elements as well as their imperfections such as, e.g., the wavelength-dependent retardance of the compensator(s). In our case, no compensator exists before the sample and $\hat{M}^{\mathrm{comp1}}$ reduces to an identity matrix. If the polarizer and analyzer are kept at fixed azimuthal angles of ±45°, it holds

$$\hat{M}^{\mathrm{pol/ana}} = \frac{1}{2}\begin{pmatrix} 1 & 0 & \pm 1 & 0 \\ 0 & 0 & 0 & 0 \\ \pm 1 & 0 & 1 & 0 \\ 0 & 0 & 0 & 0 \end{pmatrix}. \tag{A2}$$

Individual measurements "i" may still differ by, e.g., the azimuthal angle of the compensator and, hence, $\hat{M}^{\mathrm{det},i}$. The Müller matrix of a compensator that induces a retardance δ (for an ideal quarterwave plate, $\delta = 90°$) set to an azimuthal angle α_i reads

$$\hat{M}^{\mathrm{comp}}(\alpha_i) = \hat{R}^{-1}(\alpha_i)\,\hat{M}^{\mathrm{comp}}\,\hat{R}(\alpha_i), \tag{A3}$$

$$\hat{M}^{\mathrm{comp}} = \begin{pmatrix} 1 & 0 & 0 & 0 \\ 0 & 1 & 0 & 0 \\ 0 & 0 & \cos(\delta) & \sin(\delta) \\ 0 & 0 & -\sin(\delta) & \cos(\delta) \end{pmatrix}, \tag{A4}$$

$$\hat{R}(\alpha_i) = \begin{pmatrix} 1 & 0 & 0 & 0 \\ 0 & \cos(2\alpha_i) & \sin(2\alpha_i) & 0 \\ 0 & -\sin(2\alpha_i) & \cos(2\alpha_i) & 0 \\ 0 & 0 & 0 & 1 \end{pmatrix}. \tag{A5}$$

Here, $\hat{M}^{\mathrm{comp}} = \hat{M}^{\mathrm{comp}}(\alpha_i = 0)$ and $\hat{R}(\alpha_i)$ are coordinate rotation matrices.[48] However, we describe the real, imperfect compensator by its (α_i-independent) Jones matrix $\hat{J}^{\mathrm{comp}}$ and generate the respective Müller matrix using

$$\hat{M}^{\mathrm{comp}} = \hat{A}\hat{J}^{\mathrm{comp}} \otimes \hat{J}^{\mathrm{comp}^*}\hat{A}^{-1}, \tag{A6}$$

$$\hat{A} = \begin{pmatrix} 1 & 0 & 0 & 1 \\ 1 & 0 & 0 & -1 \\ 0 & 1 & 1 & 0 \\ 0 & -i & i & 0 \end{pmatrix}, \tag{A7}$$

where $\hat{J} \otimes \hat{J}^*$ is the direct tensor product of the Jones matrix and its complex conjugate.

We can rewrite Eq. (A1) by reshaping $\hat{M}^{\text{sample}}$ as 1×16 row vector $\vec{\mathcal{M}}^{\text{sample}}$ and introducing a 16×1 column vector $\vec{\mathcal{M}}^{\text{setup},i}$ such that

$$\mathcal{M}^{\text{sample}}_{4(k-1)+j} = M^{\text{sample}}_{kj}, \tag{A8}$$

$$\mathcal{M}^{\text{setup},i}_{4(k-1)+j} = M^{\text{det},i}_{1k} M^{\text{prep},i}_{j1}, \tag{A9}$$

$$I_i = \vec{\mathcal{M}}^{\text{sample}} \vec{\mathcal{M}}^{\text{setup},i}. \tag{A10}$$

An ellipsometry measurement consists of n individual measurements "i" with different azimuthal angles of certain polarization elements, e.g., the compensator. Hence, we obtain n intensity values I_i, which we store in a $1 \times n$ row vector $\vec{I}$ and define a $16 \times n$ matrix $\hat{\mathcal{M}}^{\text{setup}}$ such that every ith column is given by $\vec{\mathcal{M}}^{\text{setup},i}$ from Eq. (A9) above, for the respective partial measurement "i." Now, we get a simple matrix equation covering all partial measurements, i.e.,

$$\vec{I} = \vec{\mathcal{M}}^{\text{sample}} \hat{\mathcal{M}}^{\text{setup}}, \tag{A11}$$

which needs to be inverted. Inversion of the non-squared matrix $\hat{\mathcal{M}}^{\text{setup}}$ is mathematically equivalent to solving the least squares problem for Eq. (A11). We write the sum of squared errors, *SSE*, as

$$SSE = \left(\vec{I} - \vec{\mathcal{M}}^{\text{sample}} \hat{\mathcal{M}}^{\text{setup}}\right)^2. \tag{A12}$$

The *SSE* is minimized if its derivative with respect to $\vec{\mathcal{M}}^{\text{sample}}$ (Jacobian) turns zero,

$$\frac{\mathrm{d}SSE}{\mathrm{d}\vec{\mathcal{M}}^{\text{sample}}} = 2\vec{\mathcal{M}}^{\text{sample}} \hat{\mathcal{M}}^{\text{setup}} \hat{\mathcal{M}}^{\text{setup T}} - 2\vec{I}\hat{\mathcal{M}}^{\text{setup T}} = 0, \tag{A13}$$

$$\Leftrightarrow$$

$$\vec{\mathcal{M}}^{\text{sample}} = \vec{I}\hat{\mathcal{M}}^{\text{setup T}} \left(\hat{\mathcal{M}}^{\text{setup}} \hat{\mathcal{M}}^{\text{setup T}}\right)^{-1}. \tag{A14}$$

Hence, we obtain all 16 Müller matrix elements of the sample by this so-called Moore–Penrose pseudo-inverse.[74] It is mathematically equivalent to obtaining the Fourier coefficients from the intensity evolution upon rotating a polarization element and compute the ellipsometric angles from them.

Pseudo-inversion of $\hat{\mathcal{M}}^{\text{setup}}$ and, hence, inversion of the matrix $(\hat{\mathcal{M}}^{\text{setup}} \hat{\mathcal{M}}^{\text{setup T}})$ are only possible if the latter has a full rank, i.e., $\text{rank}(\hat{\mathcal{M}}^{\text{setup}}) = 16$. This condition is fulfilled if four linearly independent polarization states are prepared (cf. $\hat{M}^{\text{prep},i}$) and probed (cf. $\hat{M}^{\text{det},i}$). This requires two compensators. However, the formalism can be adapted if not all 16 Müller matrix elements need to be obtained independently and in the case of, e.g., only one compensator.

2. Reduction for (pseudo-)isotropic samples

For isotropic samples or samples with at least orthorhombic symmetry with their main axes aligned parallel to the laboratory coordinate system, the Müller matrix without the presence of depolarization reduces to

$$\hat{M}^{\text{sample}} = \begin{pmatrix} M^{\text{sample}}_{11} & M^{\text{sample}}_{12} & 0 & 0 \\ M^{\text{sample}}_{12} & M^{\text{sample}}_{11} & 0 & 0 \\ 0 & 0 & M^{\text{sample}}_{33} & M^{\text{sample}}_{34} \\ 0 & 0 & -M^{\text{sample}}_{34} & M^{\text{sample}}_{33} \end{pmatrix} = M^{\text{sample}}_{11} \begin{pmatrix} 1 & -N & 0 & 0 \\ -N & 1 & 0 & 0 \\ 0 & 0 & C & S \\ 0 & 0 & -S & C \end{pmatrix}. \tag{A15}$$

Hence, only four independent variables exist, and the 16 dimensions of Eq. (A11) reduce to four,

$$\vec{I}^{\text{iso}} = M^{\text{sample}}_{11}(1, N, C, S) \hat{\mathcal{M}}^{\text{setup, iso}}, \tag{A16}$$

where M^{sample}_{11} represents both light intensity and (unpolarized) reflectance or transmittance of the sample. Now, $\hat{\mathcal{M}}^{\text{setup, iso}}$ is a $4 \times n$ matrix, the ith column of which consists of the following column vector:

$$\vec{\mathcal{M}}^{\text{setup, iso},i} = \begin{pmatrix} M^{\text{det},i}_{11} M^{\text{prep},i}_{11} + M^{\text{det},i}_{12} M^{\text{prep},i}_{21} \\ -M^{\text{det},i}_{11} M^{\text{prep},i}_{21} - M^{\text{det},i}_{12} M^{\text{prep},i}_{11} \\ M^{\text{det},i}_{13} M^{\text{prep},i}_{31} + M^{\text{det},i}_{14} M^{\text{prep},i}_{41} \\ M^{\text{det},i}_{13} M^{\text{prep},i}_{41} - M^{\text{det},i}_{14} M^{\text{prep},i}_{31} \end{pmatrix}. \tag{A17}$$

It follows, subsequently, for the ellipsometric parameters,

$$M^{\text{sample}}_{11}(1, N, C, S) = \vec{I}\hat{\mathcal{M}}^{\text{setup, iso T}} \left(\hat{\mathcal{M}}^{\text{setup, iso}} \hat{\mathcal{M}}^{\text{setup, iso T}}\right)^{-1}. \tag{A18}$$

$\hat{\mathcal{M}}^{\text{setup, iso}}$ has a full rank of 4 if four linearly independent polarizations are either prepared or probed. Hence, using only one compensator is sufficient. A non-depolarizing sample, i.e., $N^2 + C^2 + S^2 = 1$, allows in principle reducing the data reduction to a rank-3 problem.

3. Reduction for (pseudo-)isotropic samples with depolarization

The simplest approach to depolarization is a sample Müller matrix, Eq. (A15), that takes a shape similar to

$$M^{\text{sample}}_{11} \begin{pmatrix} 1 & -\tilde{N} & 0 & 0 \\ -\tilde{N} & \frac{1}{1+D} & 0 & 0 \\ 0 & 0 & \tilde{C} & \tilde{S} \\ 0 & 0 & -\tilde{S} & \tilde{C} \end{pmatrix}, \tag{A19}$$

where D ($D \geq 0$) is a measure of depolarization such that $\tilde{N}^2 + \tilde{C}^2 + \tilde{S}^2 = \frac{1}{(1+D)^2} \leq 1$. This matrix is obtained by adding the Müller matrix of an ideal depolarizer, scaled by D, to Eq. (A15) and renormalize the entire Müller matrix. The respective $\tilde{N}$, $\tilde{C}$, and $\tilde{S}$ values in (A19) differ from N, C, and S in (A15) because they relate to a depolarizing sample. It holds $\tilde{X} = X/(1 + D)$, where X stands for N, C, and S.

In general, there exist now five independent parameters in the linear regression, and Eqs. (A16) and (A17) change to

$$\vec{I} = M_{11}^{\text{sample}}\left(1, \tilde{N}, \tilde{C}, \tilde{S}, \frac{1}{1+D}\right)\hat{\mathcal{M}}^{\text{setup, iso, dep}}, \tag{A20}$$

where now $\hat{\mathcal{M}}^{\text{setup, iso, dep}}$ is a $5 \times n$ matrix, and its ith column reads

$$\vec{\mathcal{M}}^{\text{setup, iso, dep},i} = \begin{pmatrix} M_{11}^{\text{det},i} M_{11}^{\text{prep},i} \\ -M_{11}^{\text{det},i} M_{21}^{\text{prep},i} - M_{12}^{\text{det},i} M_{11}^{\text{prep},i} \\ M_{13}^{\text{det},i} M_{31}^{\text{prep},i} + M_{14}^{\text{det},i} M_{41}^{\text{prep},i} \\ M_{13}^{\text{det},i} M_{41}^{\text{prep},i} - M_{14}^{\text{det},i} M_{31}^{\text{prep},i} \\ M_{12}^{\text{det},i} M_{21}^{\text{prep},i} \end{pmatrix}. \tag{A21}$$

Equation (A18) changes accordingly.

However, if the polarizer is fixed at ±45° or, such as in the measurements, the second column of the sample Müller matrix is not accessed at all, the approach of Appendix A 2 is sufficient. The degree of polarization is then expressed by

$$DOP = \sqrt{N^2 + C^2 + S^2}. \tag{A22}$$

It should be noted that Ψ and Δ are to first order unaffected by depolarization, i.e., Eqs. (5) and (6) intrinsically involve only the non-depolarizing part of the Müller matrix, which corresponds to replacing (N, C, S) by $(N, C, S)/DOP$.

APPENDIX B: JONES MATRIX OF AN IMPERFECT COMPENSATOR

Here, we discuss some of the most important literature references about compensator imperfections and consider symmetries of Jones matrices used to describe real compensators in comparison with the approach used here [Eq. (3)]. The symmetries are compared with regard to the relation of the absolute value and the phase angle of the off-diagonal elements and real or complex values of the diagonal elements. As described in Secs. III and IV, the absolute intensity is an arbitrary parameter. Hence, no attention is given to the norm of the respective Jones matrices. Neither of the wavelength dependencies is considered further here.

Plenty of literature can be found on the topic of compensator non-idealities, e.g., Refs. 38, 45, 54, 75, and 76. As mentioned above, the main imperfections are in the wavelength dependence of their retardance (especially for usage as quarterwave plates) [45,47,77] and in the orientation of the fast/slow axis (for broadband achromatic compensators, which consist of more than two plates).[45,46] Further non-idealities include dichroism (e.g., by polarization-dependent reflection losses),[52,53] optical activity,[78] and the above-mentioned spectral oscillations.[49–53] Spectral oscillations can even cause depolarization if the spectral bandwidth of the experiment is too large (i.e., the spectral resolution to low).[79] An appropriate description requires a Müller matrix approach.[47]

In the most general way, a compensator can be described by six independent parameters,[38,54]

$$\hat{J}^{\text{comp}} = \begin{pmatrix} 1 & \tan(\psi_{12}) e^{i\delta_{12}} \\ \tan(\psi_{21}) e^{i\delta_{21}} & \tan(\psi_{22}) e^{i\delta_{22}} \end{pmatrix}, \tag{B1}$$

where $\psi_{12,21,22} \approx 45°$ and $\delta_{22} \approx \pi/2$ for a quarterwave plate. In practice, proper identification of all six parameters without accidentally assigning other setup non-idealities to the compensator is difficult.

The Jones matrix of an ideal compensator was shown in Eq. (2) above and contains only one parameter (retardance δ). The first minimal adaptation is represented by[45]

$$\hat{J}^{\text{comp}} = \begin{pmatrix} 1 & 0 \\ 0 & \tan(\psi_C) e^{i\delta} \end{pmatrix}. \tag{B2}$$

Effectively, linear dichroism is described if $\psi_C \neq 45°$. Hence, polarization-dependent reflection losses can be captured in this way.

A particular effect that has been investigated is optical activity.[55,75,78] To first order, a compensator with optical activity can be described as follows (optical-activity coefficient γ_C):

$$\begin{aligned} \hat{J}^{\text{comp}} &= \begin{pmatrix} 1 & -i\gamma_C(1 - e^{+i\delta}) \\ i\gamma_C(1 - e^{i\delta}) & e^{i\delta} \end{pmatrix} \\ &\equiv \begin{pmatrix} 1 & \tan(\psi_{\text{offdiag}}) e^{i\delta_{\text{offdiag}}} \\ -\tan(\psi_{\text{offdiag}}) e^{i\delta_{\text{offdiag}}} & e^{i\delta_{\text{diag}}} \end{pmatrix}. \end{aligned} \tag{B3}$$

Accordingly, the Jones matrix is complex-valued anti-symmetric. Optical activity is inherent to quartz crystals. Such are not used in the present setup, and the shown Jones matrix representation Eq. (B3) does not apply.

Another approach for composite compensators consists in a description based on an ideal compensator plus rotation (here, by angle α_C).[56] It results in an asymmetric Jones matrix,

$$\begin{aligned} \hat{J}^{\text{comp}} &= \begin{pmatrix} \cos(\alpha_C) & \sin(\alpha_C) \\ -\sin(\alpha_C) & \cos(\alpha_C) \end{pmatrix} \begin{pmatrix} 1 & 0 \\ 0 & e^{i\delta} \end{pmatrix} \\ &\equiv \begin{pmatrix} 1 & -\tan(\alpha_C) e^{i\delta} \\ \tan(\alpha_C) & e^{i\delta} \end{pmatrix}. \end{aligned} \tag{B4}$$

In a PSCA system as the present setup, α_C can be effectively expressed by (or formally not distinguished from) an azimuthal offset angle of the analyzer.

The presently applied Eq. (3) is close to a rotated compensator with linear dichroism [Eq. (B2)],

$$\begin{aligned} \hat{J}^{\text{comp}} &= \begin{pmatrix} 1 & \tan(\psi_{\text{offdiag}}) e^{i\delta_{\text{offdiag}}} \\ \tan(\psi_{\text{offdiag}}) e^{i\delta_{\text{offdiag}}} & \tan(\psi_{\text{diag}}) e^{i\delta_{\text{diag}}} \end{pmatrix} \\ &\cong \begin{pmatrix} \cos(\alpha_C) & \sin(\alpha_C) \\ -\sin(\alpha_C) & \cos(\alpha_C) \end{pmatrix} \begin{pmatrix} 1 & 0 \\ 0 & \tan(\psi_C) e^{i\delta} \end{pmatrix} \begin{pmatrix} \cos(\alpha_C) & -\sin(\alpha_C) \\ \sin(\alpha_C) & \cos(\alpha_C) \end{pmatrix}. \end{aligned}$$

The ≅ holds because the description Eq. (3) (first line here) contains four free parameters, not only three (δ, ψ_C, and α_C). In conclusion, the description applied here incorporates four free parameters that effectively describe polarization-dependent reflection losses, orientation (rotation) of the fast/slow axis, exact induced retardance, and one more free parameter that captures, e.g., an additional rotation. The wavelength-dependent orientation of the fast/slow axis and retardance are imprinted in the Jones matrix elements, as can be seen in Fig. 6.

DATA AVAILABILITY

The data that support the findings of this study are available from the corresponding author upon reasonable request.

REFERENCES

[1]G. E. Jellison and D. H. Lowndes, Appl. Opt. **24**, 2948 (1985).
[2]D. H. Auston and C. V. Shank, Phys. Rev. Lett. **32**, 1120 (1974).
[3]R. M. A. Azzam, Thin Solid Films **234**, 371 (1993).
[4]H. R. Choo, X. F. Hu, M. C. Downer, and V. P. Kesan, Appl. Phys. Lett. **63**, 1507 (1993).
[5]J. I. Dadap, Jr., H.-R. Choo, X. F. Hu, Q. Deng, and M. C. Downer, Proc. SPIE **1861**, 285 (1993).
[6]H. Yoneda, H. Morikami, K. I. Ueda, and R. M. More, Phys. Rev. Lett. **91**, 075004 (2003).
[7]S. Zollner, K. D. Myers, K. G. Jensen, J. M. Dolan, D. W. Bailey, and C. J. Stanton, Solid State Commun. **104**, 51 (1997).
[8]S. K. Sundaram and E. Mazur, Nat. Mater. **1**, 217 (2002).
[9]J. Shah, *Ultrafast Spectroscopy of Semiconductors and Semiconductor Nanostructures*, Springer Series in Solid-State Sciences Vol. 115 2nd ed. (Springer, 1999).
[10]C. Poellmann, P. Steinleitner, U. Leierseder, P. Nagler, G. Plechinger, M. Porer, R. Bratschitsch, C. Schüller, T. Korn, and R. Huber, Nat. Mater. **14**, 889 (2015).
[11]L. Huang, J. P. Callan, E. N. Glezer, and E. Mazur, Phys. Rev. Lett. **80**, 185 (1998).
[12]J. P. Callan, A. M.-T. Kim, L. Huang, and E. Mazur, Chem. Phys. **251**, 167 (2000).
[13]C. A. D. Roeser, A. M.-T. Kim, J. P. Callan, L. Huang, E. N. Glezer, Y. Siegal, and E. Mazur, Rev. Sci. Instrum. **74**, 3413 (2003).
[14]T. Shih, M. T. Winkler, T. Voss, and E. Mazur, Appl. Phys. A **96**, 363 (2009).
[15]C.-K. Min, D. G. Cahill, and S. Granick, Rev. Sci. Instrum. **81**, 074902 (2010).
[16]T. W. Roger and A. Kaplan, MRS Proc. **1426**, 395 (2012).
[17]W. He, "Ultrafast dynamics of photoexcited carriers in semiconducting nano materials," Ph.D. thesis, University of Birmingham (2015).
[18]A. Dubietis, G. Tamošauskas, R. Šuminas, V. Jukna, and A. Couairon, Lith. J. Phys. **57**, 113 (2017).
[19]B. Lang, Rev. Sci. Instrum. **89**, 093112 (2018).
[20]S. Rapp, M. Kaiser, M. Schmidt, and H. P. Huber, Opt. Express **24**, 17572 (2016).
[21]J. Csontos, Z. Toth, Z. Pápa, B. Gábor, M. Füle, B. Gilicze, and J. Budai, Appl. Surf. Sci. **421**, 325 (2017).
[22]T. Pflug, J. Wang, M. Olbrich, M. Frank, and A. Horn, Appl. Phys. A **124**, 116 (2018).
[23]O. Herrfurth, T. Pflug, M. Olbrich, M. Grundmann, A. Horn, and R. Schmidt-Grund, Appl. Phys. Lett. **115**, 212103 (2019).
[24]F. Boschini, H. Hedayat, C. Piovera, C. Dallera, A. Gupta, and E. Carpene, Rev. Sci. Instrum. **86**, 013909 (2015).
[25]E. Baldini, A. Mann, S. Borroni, C. Arrell, F. van Mourik, and F. Carbone, Struct. Dyn. **3**, 064301 (2016).
[26]C. A. Bolme, S. D. McGrane, D. S. Moore, and D. J. Funk, J. Appl. Phys. **102**, 033513 (2007).
[27]J. Meyer-Ilse, D. Akimov, and B. Dietzek, Laser Photonics Rev. **7**, 495 (2013).
[28]K. Hiramatsu and T. Nagata, J. Chem. Phys. **143**, 121102 (2015).
[29]V. V. Kruglyak, R. J. Hicken, M. Ali, B. J. Hickey, A. T. G. Pym, and B. K. Tanner, Phys. Rev. B **71**, 233104 (2005).
[30]J. Winter, S. Rapp, M. Schmidt, and H. P. Huber, Proc. SPIE **10091**, 100910R (2017).
[31]S. Richter, O. Herrfurth, S. Espinoza, M. Rebarz, M. Kloz, J. A. Leveillee, A. Schleife, S. Zollner, M. Grundmann, J. Andreasson, and R. Schmidt-Grund, New J. Phys. **22**, 083066 (2020); arXiv:1902.05832.
[32]S. Espinoza, S. Richter, M. Rebarz, O. Herrfurth, R. Schmidt-Grund, J. Andreasson, and S. Zollner, Appl. Phys. Lett. **115**, 052105 (2019).
[33]T. Pflug, M. Olbrich, R. Roesch, U. S. Schubert, H. Hoppe, and A. Horn, Opt. Lasers Eng. **111**, 130 (2018).
[34]The Extreme Light Infrastructure (ELI) is a pan-European initiative to provide users open access to high-power lasers. Requests for the beamtime at ELI Beamlines, the Czech ELI pillar, can be issued at www.eli-beams.eu/en/users.
[35]Crossed polarizers should in general be advantageous in reflection geometry because of higher intensity throughput.
[36]P. S. Hauge and F. H. Dill, Opt. Commun. **14**, 431 (1975).
[37]It should be noted that depending on the wavelength, the white light is not necessarily polarized such as the SCG seed, especially close to the 800 nm seed.[80]
[38]W. R. Hunter, J. Opt. Soc. Am. **63**, 951 (1973).
[39]Thermal equilibration of the CCD camera requires about 1 h of continuous readout.
[40]M. Rębarz, M. Kloz, S. J. E. Herrera, and C. D. Brooks, UV-VIS-NIR femtosekundový elipsometrický systém, užitný vzor 30838, Česká republika, úřad průmyslového vlastnictví, 2017.
[41]J.-C. Diels and W. Rudolf, *Ultrashort Laser Pulse Phenomena*, 2nd ed. (Academic Press, 2006).
[42]Q. Yuan-Dong, W. Dan-Ling, W. Shu-Feng, and G. Qi-Huang, Chin. Phys. Lett. **18**, 390 (2001).
[43]S. A. Kovalenko, A. L. Dobryakov, J. Ruthmann, and N. P. Ernsting, Phys. Rev. A **59**, 2369 (1999).
[44]Z. Bor and Z. L. Horváth, Opt. Commun. **94**, 249 (1992).
[45]P. S. Hauge, J. Opt. Soc. Am. **68**, 1519 (1978).
[46]B. D. Johs and D. W. Thompson, "Regression calibrated spectroscopic rotating compensator ellipsometer system with photo array detector," U.S. Patent 5,872,630 (February 16 1999).
[47]B. D. Johs and C. M. Herzinger, "Regression calibrated spectroscopic rotating compensator ellipsometer system with pseudo-achromatic retarder system," U.S. Patent 6,353,477 (March 5, 2002).
[48]H. Fujiwara, *Spectroscopic Ellipsometry, Principles and Applications* (Wiley, 2007).
[49]D. K. Aitken and J. H. Hough, Publ. Astron. Soc. Pac. **113**, 1300 (2001).
[50]K. Ebert and D. E. Aspnes, Thin Solid Films **455-456**, 779 (2004).
[51]P. Marsik and J. Humlicek, Phys. Status Solidi C **5**, 1064 (2008).
[52]H. Weinberger and J. Harris, J. Opt. Soc. Am. **54**, 552 (1964).
[53]H. T. Yolken, R. M. Waxler, and J. Kruger, J. Opt. Soc. Am. **57**, 283 (1967).
[54]R. M. A. Azzam and N. M. Bashara, J. Opt. Soc. Am. **61**, 1236 (1971).
[55]D. E. Aspnes, J. Opt. Soc. Am. **64**, 812 (1974).
[56]H. Gu, S. Liu, X. Chen, and C. Zhang, Appl. Opt. **54**, 684 (2015).
[57]A. Savitzky and M. J. E. Golay, Anal. Chem. **36**, 1627 (1964).
[58]V. L. Le, T. J. Kim, Y. D. Kim, and D. E. Aspnes, J. Vac. Sci. Technol., B **37**, 052903 (2019).
[59]R. A. Chipman, "Polarimetry," in *Handbook of Optics* (McGraw-Hill, 1995), Chap. 22.
[60]O. Herrfurth, "Development of a femtosecond time-resolved spectroscopic ellipsometry setup," M.S. thesis, Universität Leipzig, 2017, http://nbn-resolving.de/urn:nbn:de:bsz:15-qucosa2-347203.
[61]Same conditions means data taken from the same sample at the same angle of incidence and also with a similar spectral bandwidth. In case the spectral bandwidth of the reference measurement is smaller than that in the experiment, a respective convolution can be applied to the reference spectra. In fact, reference spectra can also be computed if the sample is known sufficiently well, e.g., from ellipsometry measurements at different angles.
[62]B. Johs and J. S. Hale, Phys. Status Solidi A **205**, 715 (2008).
[63]D. W. Berreman, J. Opt. Soc. Am. **62**, 502 (1972).
[64]M. Schubert, Phys. Rev. B **53**, 4265 (1996).
[65]S. Zollner, K. D. Myers, J. M. Dolan, D. W. Bailey, and C. J. Stanton, Thin Solid Films **313-314**, 568 (1998).
[66]P. Koleják, "Specific aspects of terahertz time-domain spectroscopy," Bachelor thesis, Technická Univerzita Ostrava, 2018, http://hdl.handle.net/10084/130270.
[67]H. Kano and T. Kobayashi, Opt. Commun. **178**, 133 (2000).
[68]H. N. Yum and M. S. Shahriar, J. Opt. **12**, 104018 (2010).
[69]K. Elk and W. Gasser, *Die Methode der Greenschen Funktionen in der Festkörperphysik* (Akademie-Verlag, Berlin, 1979).

[70]M. A. M. Versteegh, T. Kuis, H. T. C. Stoof, and J. T. Dijkhuis, Phys. Rev. B **84**, 035207 (2011).
[71]S. Espinoza, G. Neuber, C. D. Brooks, B. Besner, M. Hashemi, M. Rübhausen, and J. Andreasson, Appl. Surf. Sci. **421**, 378 (2017).
[72]S. Espinoza, F. Samparisi, F. Frassetto, S. Richter, M. Rebarz, O. Finke, M. Albrecht, M. Jurkovic, O. Hort, N. Fabris, A. Zymaková, D. D. Mai, R. Antipenkov, J. Nejdl, L. Poletto, and J. Andreasson, J. Vac. Sci. Technol., B **38**, 024005 (2020).
[73]D. Wegkamp, D. Brida, S. Bonora, G. Cerullo, J. Stähler, M. Wolf, and S. Wall, Appl. Phys. Lett. **99**, 101101 (2011).
[74]A. Ben-Israel and T. N. E. Greville, *Generalized Inverses* (Springer, 2003).
[75]R. Kleim, L. Kuntzler, and A. El Ghemmaz, J. Opt. Soc. Am. A **11**, 2550 (1994).
[76]J. Lee, P. I. Rovira, I. An, and R. W. Collins, J. Opt. Soc. Am. A **18**, 1980 (2001).
[77]I. An, J. A. Zapien, C. Chen, A. S. Ferlauto, A. S. Lawrence, and R. W. Collins, Thin Solid Films **455-456**, 132 (2004).
[78]D. E. Aspnes, Appl. Opt. **10**, 2545 (1971).
[79]P. Koleják, D. Vala, K. Postava, P. Provazníková, and J. Pištora, J. Vac. Sci. Technol., B **38**, 014006 (2020).
[80]I. Buchvarov, A. Trifonov, and T. Fiebig, Opt. Lett. **32**, 1539 (2007).
[81]For further discussions here, the intensity profile is confined along one dimension like for a slit aperture. By contrast, the intensity contained in a circular aperture defined by the $1/e^2$ diameter or the FWHM are 86% and 50%, respectively (two-dimensional confinement).